Chemical Engineering Journal 453 (2023) 139719

Contents lists available at ScienceDirect

Chemical Engineering Journal

journal homepage: www.elsevier.com/locate/cej

Validation and evaluation of the CPFD modeling of dense particle flow velocity: Taking particle flow around an obstacle as an example

Xiandong Liu, Hai Zhang, Hairui Yang, Yang Zhang *, Junfu Lyu

Key Laboratory for Thermal Science and Power Engineering of Ministry of Education, Department of Energy and Power Engineering, Tsinghua University, Beijing 100084, China

ARTICLE INFO

Keywords:
Dense particle flow
Flow around an obstacle
Stained-particle image velocimetry
Computational particle fluid dynamics
Particle velocity distribution

ABSTRACT

The computational particle fluid dynamic (CPFD) method is a common approach to simulating dense particle flow, but the direct validation of the CPFD model using the particle velocity distribution is lacking. Taking particle flow around an obstacle as an example, the accuracy of the CPFD method in the simulation of the dense particle velocity field was validated and evaluated in the present study. The particle flow field was experimentally visualized using a quasi-2D flow channel and the particle velocity distribution was measured by a newly-proposed stained-particle image velocimetry technique. The simulated particle velocity using the CPFD method was compared with the measured data and the results indicated that the CPFD method was capable of accurately predicting the particle flow velocity distribution as well as the overall parameters such as the apparent mass flux if the CPFD model parameters were properly adopted. The sensitivity analysis of the simulated particle velocity to the key CPFD parameters was conducted and the results showed that the simulated particle velocity distribution was quite sensitive to the particle pack volume fraction, while the particle stress model parameters and particle-to-wall restitution coefficients show less and close sensitivity in the dense particle flow situations. The recommended model parameters were given in the present study. It is also found that multiple choices of the model parameter combinations could all give accurate overall mass flow predictions but might lead to very different flow velocity distributions with a prediction error even higher than 45%. One should directly verify the CPFD simulated flow velocity using the experimental data if the flow field study was desired.

1. Introduction

The phenomenon of dense particle flow is commonly seen in industrial processes (*e.g.*, chemical engineering, metallurgy, power engineering, *etc.* [1–3]). Numerous studies have been conducted to understand the governing mechanism of this phenomenon, but some aspects still have not been fully explored. To obtain a deeper insight into the dense particle flow behavior and its underlying physics, the numerical simulation has become an essential tool, not only due to its low cost of the flexible selection of operating conditions but also because it can provide all kinds of inner flow details which are usually not easily measured in the experiments. Recently, more and more numerical simulation studies have been conducted to understand the dense particle flow behavior in the literature.

Many different numerical methods have been developed and applied in the dense particle flow simulation. These methods include the direct numerical simulation method (DNS) [4], the discrete element method (DEM) [5], the computational particle dynamics method (CPFD) [6], the kinetic method [7], the two-fluid method (TFM) [8], *etc.* Different numerical methods rely on different physical assumptions, while more detailed and elaborate models usually lead to better prediction accuracies but higher calculation costs [9]. For a certain application, the appropriate numerical method is usually chosen as per the trade-off between prediction accuracy and cost. Among the above-mentioned method, the CPFD method has attracted increasing attention in the last decade, and has been widely chosen for the simulation of dense particle flow in a group of large-scale equipment (*e.g.*, circulating fluidized bed [10], downer reaction [11], gasifier [12], *etc.*) as the CPFD method greatly reduces simulation cost while still hold some key particle flow characteristics.

It is always necessary to use experimental data to verify the validity of the numerical models in the first place. Among existing CPFD simulation studies, the experimental data of some flow overall parameters, such as the overall mass flow rate, pressure, temperature, and particle

* Corresponding author.
E-mail address: yang-zhang@tsinghua.edu.cn (Y. Zhang).

https://doi.org/10.1016/j.cej.2022.139719
Received 26 July 2022; Received in revised form 20 September 2022; Accepted 7 October 2022
Available online 13 October 2022

concentration, were commonly used for the CPFD model validation. For instance, Nie et al. [13] used the outflow mass flow rate of a solid particle solar receiver as a target parameter to prove the accuracy of their CPFD model, and the particle velocity distribution in the equipment was subsequently investigated using this model. Jin et al. [14] applied the measured pressure drop of a tube to validate their CPFD model and the gas–solid flow state was thereby studied using the optimized model parameters. The pressure spectral density and particle volume fraction were used in Córcoles et al.'s study [15] to validate the CPFD simulation of the bubble behavior in a bubbling fluidized bed. Jia et al. [16] verified the accuracy of the CPFD modeling of a CFB boiler based on the experimental results of the temperature at a series of measurement points along the circulation loop, and the verified model was applied to study the distribution of the furnace temperature and particle velocity.

Among the existing CPFD simulation studies, the distribution of the particle velocity is crucial and frequently discussed [17,18], while the accuracy of the CPFD simulation of the particle velocity has been seldom directly validated using experimental data. It's questionable whether the CPFD models optimized using only the overall parameters, such as the total particle flow rate, the temperature, the pressure drop, *etc.*, can accurately predict the particle velocity distribution. It is found (to be shown in Section 4.3) that multiple model parameter combinations can provide satisfactory predictions of the aforementioned overall parameters. Meanwhile, it's also worth considering whether, and how great, discrepancies among the simulated velocity distributions may be produced using different model parameter combinations.

The accurate experimental data of the particle flow velocity and its distribution are the basis for CPFD model validation. The precise measurements of the dense particle flow velocity distribution are challenging and have attracted continuous efforts in the literature. The optical measurement method is often adopted for particle velocimetry as the particle trajectory can be recorded by the high-speed camera and thereby the particle velocity is obtained. For example, Chehata et al. [19] obtained the particle velocity distribution of glass beads with diameters of 3 mm and 6 mm using the high-speed camera technique. Using similar methods, the velocity fields of particles made of alumina oxide, zeolite, and polyurethane disk were also studied in the literature [20,21]. In addition to the high-speed camera technique, the three-dimensional X-ray technique was also applied to capture the particle velocity [22]. The existing experimental measurements of the dense particle flow field are still limited to flows with relatively large particles whose diameters are larger than 1.5 mm. Normally these particles fall in the category of Group D in Geldart's classification [23]. However, the flow field of smaller particles, such as the flows consisting of $\sim$ 100 μm particles (normally Geldart Group A or B particles), are also important and commonly seen in the industry, while experimental measurements of dense particle flows with particle diameter being in the order of 100 μm are still rarely seen in the literature. There are experimental studies in which the optical measurements were applied to such small particles, but the gas bubble behavior [24] or the bed expansion [25] were captured, rather than the particle velocity. As the CPFD modeling is frequently applied to dense particle flows with particle diameters around 100 μm (*e.g.*, [26,27]), it is important to develop techniques of dense particle flow velocity measurements in the same particle diameter range to solidly prove the availability of using CPFD model simulating the dense particle flow field.

For this study, new experimental measurements of the dense particle flow field were conducted and the accuracy of dense particle flow field simulation using the CPFD model was discussed. Flow around an obstacle is an important subject as it provides a benchmark to investigate many important flow problems, such as drag force, boundary layer, eddy formation, *etc*. Thus, the downward dense particle flow around an obstacle was adopted as a benchmark in the present study. A stained particle image velocimetry (SPIV) technique was developed to measure the particle velocity distribution around the obstacle. The corresponding CPFD modeling was also conducted using different model parameters. The errors of the velocity distribution predictions using different model parameters were evaluated and suggestions for the model parameter adoption were also given.

2. Experimental approach

The dense particle flow around an obstacle was adopted as the research object in the present study. The particle velocity field around the obstacle was quantitatively measured. To visualize the particle flow, a quasi-two-dimensional (quasi-2D) flow channel configuration integrated with the optical measurement technique was established. Its details were given in this section.

2.1. Apparatus

The experimental system is schematically shown in Fig. 1. The core part of this rig was a vertically-placed flow channel with a height of 400 mm. The core flow channel was set as a quasi-2D configuration to provide an observation plane for photography. The size of the horizontal cross-section of the flow channel was 160 mm $\times$ 15 mm. As the length (160 mm) of the cross-section was overwhelmingly greater than the width (15 mm), the particle velocity profile was assumed to be uniform across the width of the channel and thus the vertical particle flow was regarded as quasi-2D, as shown in Fig. 1(a). Similar quasi-2D particle flow set-ups can be also found elsewhere (*e.g.*, [28,29]). The walls of the flow channel were made of glass to allow the observation of the flow and avoid the electrostatic effect between particles and walls. Obstacles of different sizes and shapes were installed in the center of the measurement section, and the dense particle flows around the obstacles were the target to validate the CPFD model. A silo was connected to the top of the channel to feed the particles. An L-valve was installed at the bottom of the channel. The fluidization air, provided by an air compressor, was distributed using the L-value to fluidize the particles and control the outflow apparent mass flux,$\dot{m}$. The outlet particles were collected by a bucket placed on an electronic scale, so the real-time accumulated particle mass was measured, and thereby the real-time particle mass flux was calculated. A high-speed camera (Module: PCO Dimax HS2, with a lens of AF Micro-Nikkor 60 mm f/2.8D) was installed to observe particle flow behaviors, and a spotlight was set as the light source, as shown in Fig. 1(b).

The experimental particles were transparent glass beads mixed with red-stained glass beads as tracers (to be explained in detail in Section 2.2). The true density of the two glass beads is 2474 kg/m^3 and the bulk density of the mixture was 1462 kg/m^3. Two types of flow materials were mixed first and then sieved together to keep the same size distribution as shown in Fig. 1(c). The average diameter of the particles (d_{50}) was 106.7 μm. As the shape of the stained glass beads, indicated by the scanning electron microscope pictures shown in Fig. 1(d) and (e), were quite similar to those of the transparent glass beads, the stained glass beads were able to trace the bulk particle flow and the error between the velocities of the transparent and stained glass beads was ignorable.

2.2. Flow observation and acquirement of the flow field

It is difficult to recognize the small particle trajectory in a dense particle flow using high-speed camera photography. To overcome this difficulty, a stained particle image velocimetry (SPIV) technique was proposed in the present study. As the number of the red-stained glass beads was one order of magnitude less than that of the main material (transparent glass beads), the location and movement of red-stained particles can be easily recognized using high-speed photography.

In this study, the real-time accumulated particle mass as a function of time was measured and the results were shown in Fig. 2. The quasi-steady state of the flow was maintained for at least 10 s. In the experiment, the observation using the high-speed camera started 5 s after the particle flow started to make sure that the observation was at a quasi-

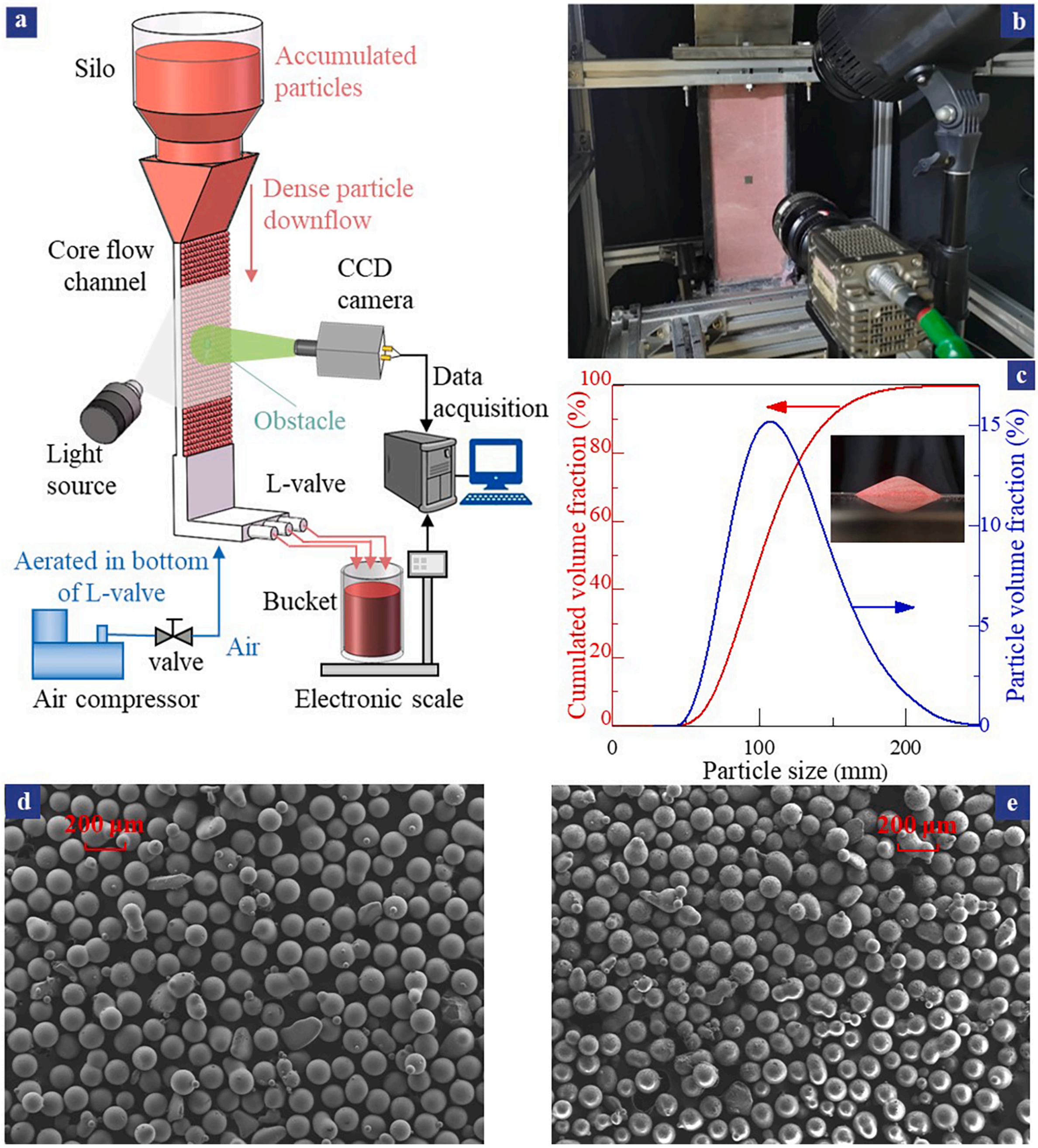

Fig. 1. Experimental system. (a). Schematic diagram of the measurement system, (b). Real picture of the measurement system apparatus, (c). Size distribution of experiment materials, (d) and (e). Scanning electron microscope picture of the transparent glass beads and red-stained glass beads.

steady state. The high-speed camera filmed 1000 fps at a resolution of 1400 × 1050. The investigation time was 1 s and 1000 frames were captured for each working condition. Taking the dense particle flow around a triangle obstacle as an example, the particle flow field visualization process was given in Fig. 3. A video of the flow observation is also given in the Supplementary Material. The original colored image was given in Fig. 3(a). To capture the red particle position, the color segmentation was applied to the picture and the pixels which met the red color threshold were viewed as tracer particles. The color segmentation was based on HSV color space and the applied threshold is shown in Table.1. Through a further binarization process, the particle image was then obtained, as shown in Fig. 3(b).

A similar particle recognition process was applied to the picture in the time series. Then, the binarized image series were processed using the software PIVLab [30] in MATLAB to obtain the particle velocity distribution. The cross-correlation method with the fast Fourier transform algorithm was applied. Four passes, where the interrogation areas were 64 × 64, 32 × 32, 16 × 16, and 8 × 8 pixels respectively, were used for the data processing. The resulted 2-dimensional vector diagram and the streamline diagram are shown in Fig. 3(c) and (d). Following the measurement processes above, the flow field of dense particle flow around any obstacle can be captured for the subsequent CPFD model validation.

3. Numerical approach

3.1. Governing equations

The CPFD method is a Eulerian-Lagrangian simulation method where the gas phase is viewed as a continuous phase and the particle

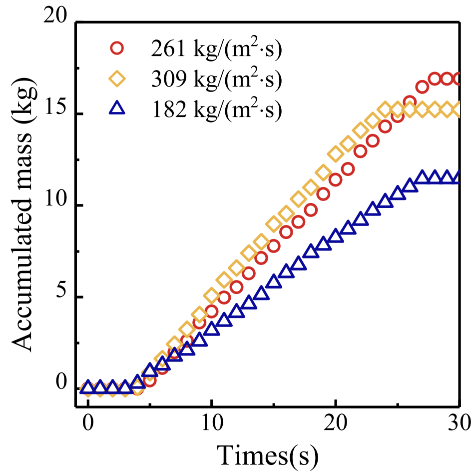

Fig. 2. Real-time accumulated particle mass versus time at different mass fluxes.

phase is viewed as a discrete phase.

For the gas phase, the continuity equation is.

$$\frac{\partial(\varepsilon_g\rho_g)}{\partial t}+\nabla\cdot(\varepsilon_g\rho_g v_g)=0 \tag{1}$$

whereε_g,ρ_g, v_g are volume fraction, density, and velocity of the gas phase, respectively.

The gas-phase momentum equation is.

$$\frac{\partial(\varepsilon_g\rho_g v_g)}{\partial t}+\nabla\cdot(\varepsilon_g\rho_g v_g v_g)=-\varepsilon_g\nabla p+\nabla\cdot\tau_g+\varepsilon_g\rho_g g-F \tag{2}$$

where p is the gas pressure and the term "$-\varepsilon_g\nabla p$" represents gas pressure gradient force; $\boldsymbol{\tau}_g$ is the gas stress tensor and the term "$\nabla\cdot\boldsymbol{\tau}_g$" represents contact force on the control volume; $\boldsymbol{g}$ is the gravitational acceleration and the term "$\varepsilon_g\rho_g\boldsymbol{g}$" is the gravity force; $\boldsymbol{F}$ is interaction force per unit volume between gas and particle phases. For a cold state simulation, the energy equation is not considered.

The turbulence model applied in CPFD simulation is the large-eddy simulation (LES). The fluid velocity and pressure are correlated by a semi-implicit pressure correction equation derived from mass conservation equations. The solving method is the SIMPLE algorithm.

For the particle phase, the probability function f is introduced to describe the average number of particles per unit volume, which indicates particle distribution. The transport equation of f is:

$$\frac{\partial f}{\partial t}+\nabla_x\cdot(v_p f)+\nabla_{v_p}\cdot(A_p f)=\frac{f_D-f}{\tau_D} \tag{3}$$

where $\boldsymbol{x}$ is the particle spatial position,v_p, ρ_p and m_p the velocity, density, and mass of the particle, t the current time, $\boldsymbol{A}_p$ the particle acceleration speed, f_D the probability density function for the local mass-averaged particle velocity, and τ_D the collision damping time.

The particle acceleration speed is described by:

$$\boldsymbol{A}_p = \frac{d\boldsymbol{v}_p}{dt}=D_p(\boldsymbol{v}_g-\boldsymbol{v}_p)-\frac{1}{\rho_p}\nabla p+\boldsymbol{g}-\frac{1}{\varepsilon_p\rho_p}\nabla\cdot\boldsymbol{\tau}_p \tag{4}$$

where ε_p is the volume fraction of particle phase, $\boldsymbol{\tau}_p$ the particle normal stress, and D_p the inter-phase drag force coefficient. The four terms on the right-hand side in Eq. (4) represent the influence of the gas–solid drag force, pressure gradient force, gravitational force, and particle collision force respectively.

The gas–solid drag model used in this work was the WenYu-Ergun model expressed as Eqs (5)–(8).

WenYu model:

$$D_1=0.75C_d\frac{\rho_g}{\rho_p}\frac{|\boldsymbol{v}_g-\boldsymbol{v}_p|}{d} \tag{5}$$

where,

$$C_d=\begin{cases}(24/Re)\varepsilon_g^{-2.65}, & Re<0.5\\ (24/Re)(1+0.15Re^{0.687})\varepsilon_g^{-2.65}, & 0.5\leqslant Re\leqslant 1000\\ 0.44\varepsilon_g^{-2.65}, & Re>1000\end{cases} \tag{6}$$

Ergun model:

$$D_2=(\frac{180\varepsilon_p}{\varepsilon_g Re}+2)\frac{\rho_g}{\rho_p}\frac{|\boldsymbol{v}_g-\boldsymbol{v}_p|}{d} \tag{7}$$

WenYu-Ergun model:

$$D_p=\begin{cases}D_1, & \varepsilon_p<0.75\varepsilon_{cp}\\ \dfrac{\varepsilon_p-0.85\varepsilon_{cp}}{0.85\varepsilon_{cp}-0.75\varepsilon_{cp}}(D_2-D_1)+D_1, & 0.75\varepsilon_{cp}\leqslant\varepsilon_p<0.85\varepsilon_{cp}\\ D_2, & \varepsilon_p>0.85\varepsilon_{cp}\end{cases} \tag{8}$$

where ε_{cp} is the particle volume fraction at the packing limit.

The model of $\boldsymbol{\tau}_p$ in the CPFD simulation was the Harris & Crighton model as Eq. (9).

Table 1
Parameter for extraction of tracer based on HSV color space.

Parameter	Lower limit	Upper limit
Hue	0.000	0.020
Saturation	0.500	0.600
Value	0.200	0.950

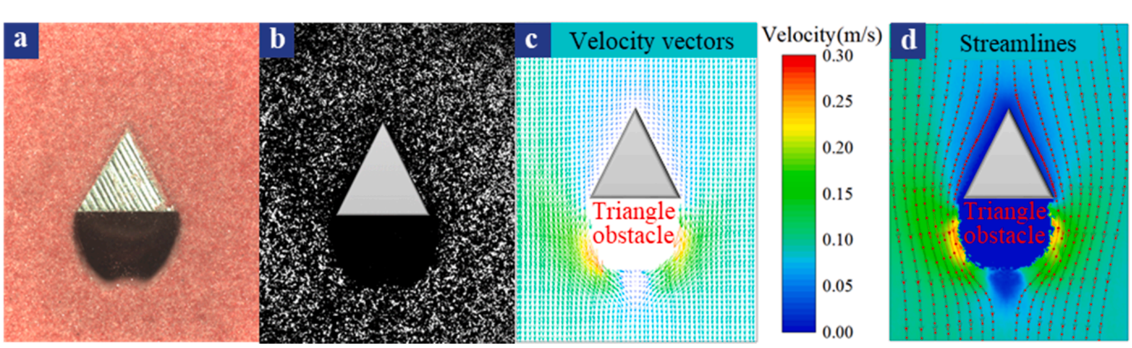

Fig. 3. Pictures showing the SPIV technique. (a) Original direct picture of high-speed photography, (b) Picture after the binarization to determine particle position, (c) Velocity vector diagram after the cross-correlation algorithm, and (d) Particle streamlines and contours of particle velocity.

$$\tau_p = \frac{p_s \varepsilon_p^{\beta}}{\max[(\varepsilon_{cp} - \varepsilon_p), \zeta(1 - \varepsilon_p)]} \tag{9}$$

where p_s is a model parameter depending on the material. $\beta = 2 - 5$ is recommended in the model and ζ is a small number to eliminate the computation singularity.

3.2. Simulation setup

The CPFD simulation was carried out based on the software Barracuda® 17.4.0. The geometry structure of the computation domain (as shown in Fig. 4(a)) was a 1:1 scaled model of the experimental rig discussed in Section 2.1. The mesh generation of the core flow channel is shown in Fig. 4(b). The pressure boundaries were set at 101325 Pa on the top plane of the silo and the outlet plane of the L-valve. The bottom plane of the L-valve was the flow boundary whose flux was set to be consistent with the experiments. The different types of obstacles were applied in the central part of the core flow channel to provide different dense particle flows. The vertical plane away from the particle outlet inside the core flow channel was used as the target research plane. The time interval was 0.0005 s and the total simulation time was 20 s. Through mesh independency analysis, the reasonable number of grids and corresponding computation particle numbers were 1.9×10^6 and 3.6×10^6, respectively.

4. Results and discussion

4.1. Flow velocity distribution of the dense particle flow around obstacles and validation of the CPFD simulation

Fig. 5 presents the colored pictures by the direct photography of dense particle flows around different obstacles. The exposure time t_e was 0.1 s to show the time-lapse of the particle movements. Videos of the particle motion can be also found in the Supplementary material. Taking the case of the dense particle flow around a cylindrical obstacle as an example (Fig. 5(a)), three distinctive zones, *i.e.*, the flow stagnant zone, the slip-shear flow zone, and the flow separation zone, around the obstacle were identified. Some particles accumulate and stagnate on top of the obstacle (the upwind side of the obstacle), forming a triangle flow stagnant zone. This phenomenon was also found in non-fluidized granular flow around the cylindrical obstacle in other literature (*e.g.*, [31]). On the sidewall of the cylinder, particles slip along the wall, forming the slip-shear flow zone. On the downstream side, the flow separation zone was observed, demonstrating an analogical phenomenon with that in the continuous fluid flowing around the cylinder process [32]. Although the obstacle shapes, size, and flow velocities are quite different in the present study, the key features of the particle flow behavior are similar and the three distinctive zones are also exhibited in Fig. 5(b–e).

The accuracy of the CPFD method simulating dense particle flow field was validated using the measured particle velocity distribution. Among the aforementioned three distinctive flow zones, the particle slip-shear flow along the sidewall is interesting for the quantitative depiction of the particle flow field (*e. g.*, [33,34]) and lateral particle velocity distribution is a widely-adopted characterized indicator for the model validation (*e. g.*, [35,36]). Therefore, the particle velocity vectors and vertical velocity in the lateral direction were adopted to validate the CPFD simulation and the experimental and numerical overall apparent mass flux was also compared as well. The dense particle flow around the cylindrical obstacle at three different apparent mass fluxes, 309 kg/(m^2·s), 261 kg/(m^2·s), and 182 kg/(m^2·s), and that around the plate obstacle at 273 kg/(m^2·s), were taken as the validation working conditions, as shown in Table 2. The characteristic length L represents the cylinder diameter for the cylinder cases and the side length for the plate case. Fig. 6 gives the validation results. The comparison of flow velocity vectors between experimental (Fig. 6(a)) and numerical (Fig. 6(b)) results indicates that the simulation can reproduce the key flow features mentioned above, although there exists some quantitative deviation. Taking velocities in the lateral direction as the quantitative validation parameter, Fig. 6(c) shows that the simulated vertical velocities generally agree well with the experimental data as the simulation reproduces the non-monotonic curves of the velocities and the peak locations. The consistency between experimental and numerical results of the flow

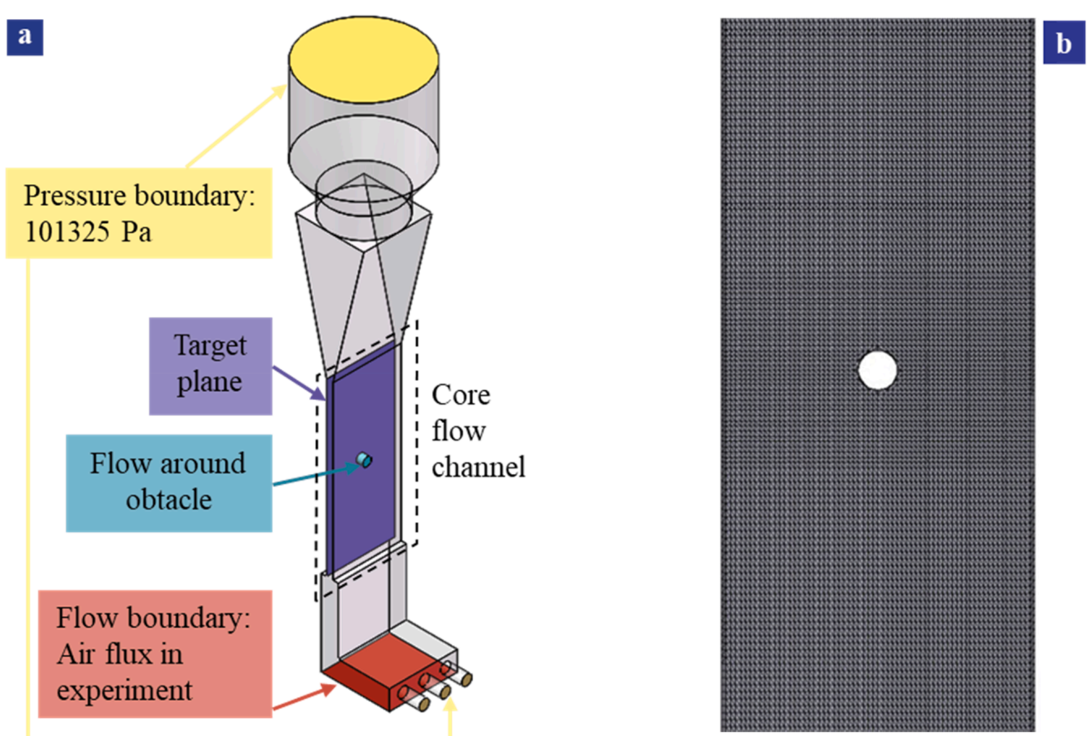

Fig. 4. Setup of the CPFD simulation. (a) Geometry model of the computation domain. (b) Mesh of the core flow channel.

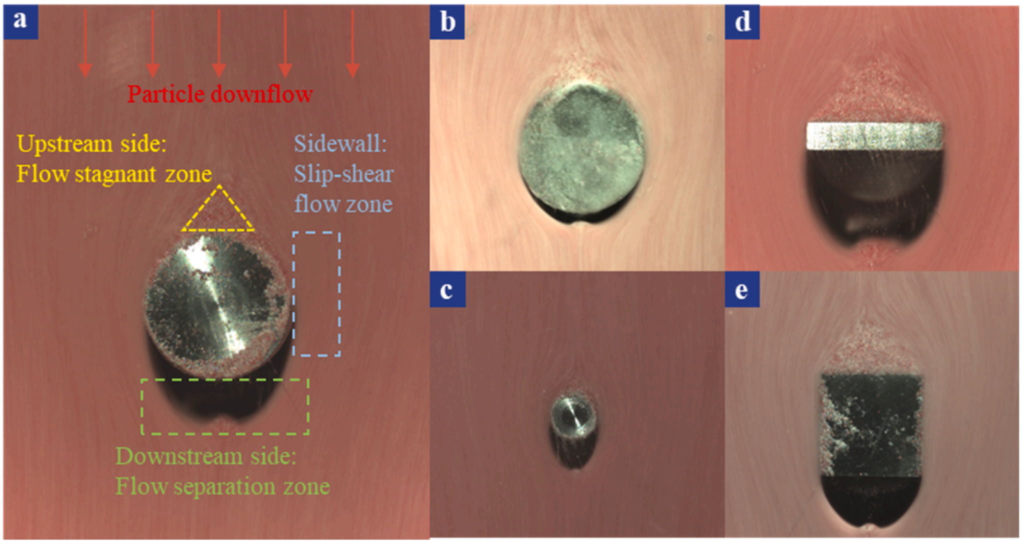

Fig. 5. Flow characteristics of dense particle flow around process based on long exposure pictures (t_e = 0.1 s). (a) Flow stagnant zone, slip-shear flow zone, and flow separation zone. Diameter of the cylindrical obstacle: 20 mm, apparent mass flux: 150 kg/(m^2·s). (b) Diameter of the cylindrical obstacle: 20 mm, apparent mass flux: 96 kg/(m^2·s). (c) Diameter of the cylindrical obstacle: 5 mm, apparent mass flux: 138 kg/(m^2·s). (d) Plate obstacle, apparent mass flux: 183 kg/(m^2·s). (e) Cube obstacle, apparent mass flux: 150 kg/(m^2·s).

Table 2
Simulation cases for the CPFD model validation.

Case	Obstacle	Experimental apparent mass flux	Simulated apparent mass flux
1	20 mm cylinder	261 kg/(m^2·s)	266 kg/(m^2·s)
2	20 mm cylinder	309 kg/(m^2·s)	305 kg/(m^2·s)
3	20 mm cylinder	182 kg/(m^2·s)	175 kg/(m^2·s)
4	19 mm plate	273 kg/(m^2·s)	275 kg/(m^2·s)

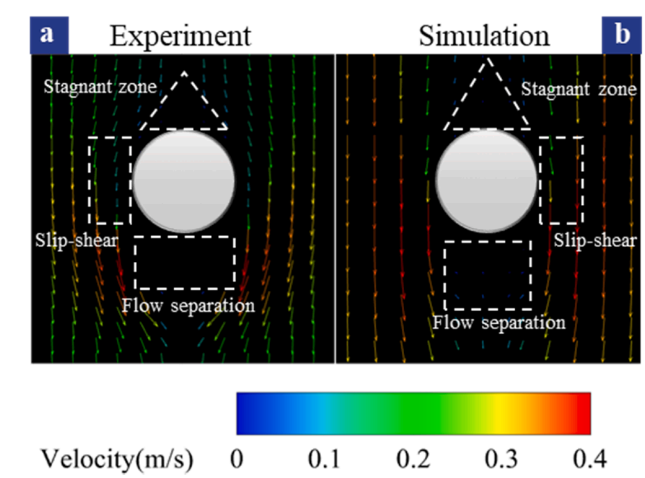

Fig. 6. Validation of the CPFD simulation accuracy using experimental data. △: Obstacle: 20 mm cylinder, $\dot{m}$= 261 kg/(m^2·s), solid line: simulation; ◇: Obstacle: 20 mm cylinder, $\dot{m}$= 309 kg/(m^2·s), dash double-dotted line: simulation; □: Obstacle: 20 mm cylinder, $\dot{m}$= 182 kg/(m^2·s), dash-dotted line: simulation; ○: Obstacle: 19 mm plate, $\dot{m}$= 273 kg/(m^2·s), dash line: simulation. (a) Experiment flow velocity vectors of Case 2: particle flow around 20 mm cylinder with the mass flux of 309 kg/(m^2·s); (b) Simulated flow field velocity vectors of Case 2; (c) Comparison of vertical velocities in the lateral direction between experimental and numerical results.

field indicates that the CPFD modeling can well simulate the whole flow field. The involved model parameters in the validation cases are provided in Table 3. The following sections discuss the influence of these parameters on the prediction of the apparent mass flux and velocity distribution.

Table 3
Parameters for the CPFD model simulating the particle velocity distribution.

Physical quantity	Parameter	value
Particle stress	p_s	100
	β	3
	ζ	1 × 10^{-7}
Gas-solid drag model		Wen Yu-Ergun
Particle-to-wall interaction	Normal-to-wall momentum retention	0.90
	Tangent-to-wall momentum retention	0.99
Close pack volume fraction ε_{cp}		0.60

4.2. Influence of some key model parameters

The particle stress model (Harris & Crighton model) dealing with particle–particle force in the CPFD method is crucial to accurately simulate the particle motion. In the particle stress model (Eq. (9)), p_s and β are two key parameters. Case 1 in Table 2 was adopted as a standard working condition to investigate the influences of p_s and β on the simulation results. The p_s range in the simulation in the present study was 1 – 100, being consistent with those in the literature (*e.g.*, [37,38]), and the β range is 2 – 5. The vertical velocity distribution along the lateral direction was the validation parameter and the experimental and numerical apparent mass flux $\dot{m}$ was also compared as many other studies did. The results are shown in Fig. 7. It can be seen that both p_s and β considerably affect the numerical results, indicating that the particle stress models are important to simulate the particle flow behavior. Especially, for the velocity distribution as shown in Fig. 7(a) and (c), p_s and β not only influence the value of the velocity but also the distribution trend. To quantitatively depict differences in the velocity distribution trend, a dimensionless parameter, k, was defined by Eq. (10) as the ratio of the peak value of the vertical velocity near the cylinder wall, v_{peak}, to the stable velocity far away from the cylinder, v_{far}.

$$k = \frac{v_{peak}}{v_{far}} \tag{10}$$

A higher k means a higher velocity peak near the wall and a larger disturbance caused by the cylindrical obstacle. Fig. 7(b) presents that k increases as p_s decreases, indicating that larger p_s results in flatter velocity distribution. The simulated apparent mass flux ($\dot{m}$) increases as p_s

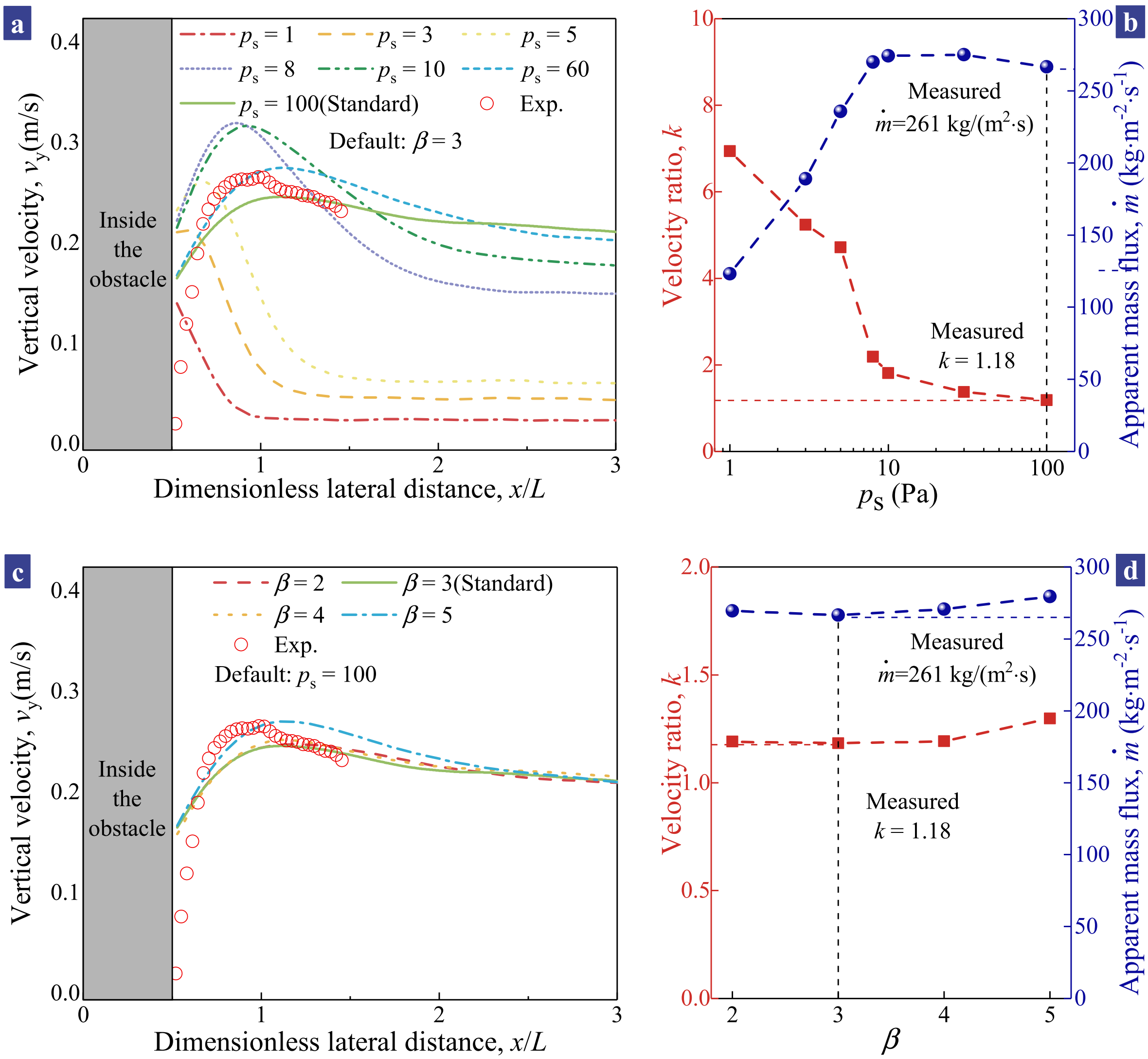

Fig. 7. Influence of particle stress model parameters on the simulation of the dense particle flow behavior. (a), (c) Influence of p_s and β on the particle velocity distribution simulation. (b), (d) Simulated and measured velocity ratio k and apparent mass flux $\dot{m}$ at different p_s's and β's.

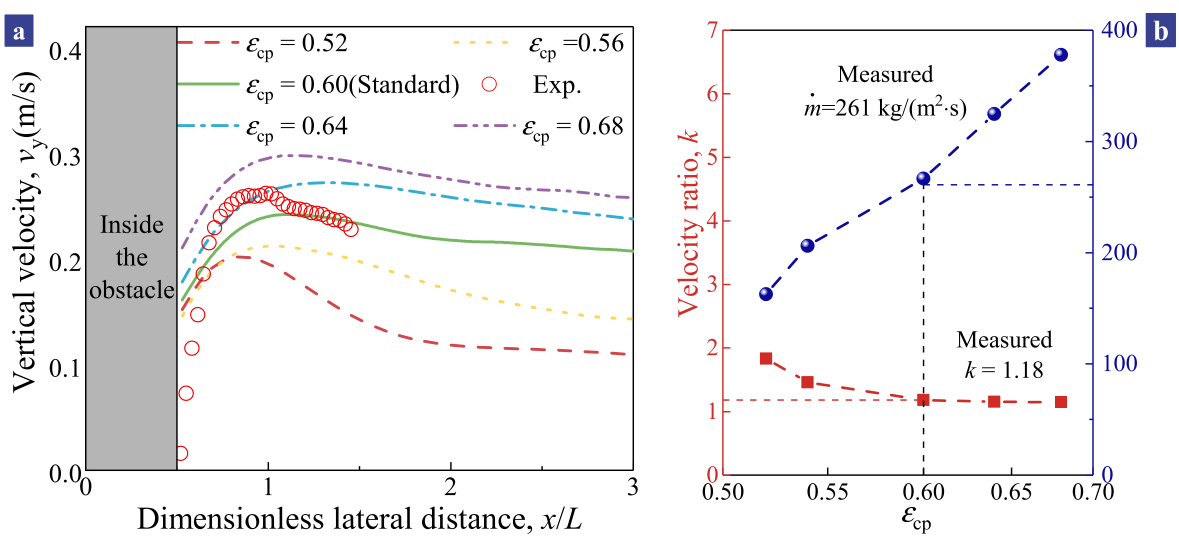

Fig. 8. Influence of the particle close pack volume fraction ε_{cp} on the dense particle flow prediction. (a) Influence of ε_{cp} on the particle velocity distribution simulation. (b) Simulated and measured velocity ratio k and apparent mass flux $\dot{m}$ at different ε_{cp}'s.

increases when p_s is comparatively small, while $\dot{m}$ changes little as p_s increases when p_s is relatively large. Fig. 7(d) shows that both k and $\dot{m}$ barely changes as β increases until β is greater than 5. The simulated values of both k and $\dot{m}$ have their best estimations at $p_s = 100$ and $\beta = 3$.

The particle close pack volume fraction ε_{cp} is defined as the maximum particle volume fraction under the randomly packed state. ε_{cp} is also an important parameter in the CPFD simulation [39]. The influence of ε_{cp} on the prediction of velocity distribution and the apparent mass flux was also investigated and the results are shown in Fig. 8. The changing scale of ε_{cp} in the simulation is 0.52–0.68, which covers the experimental estimated ε_{cp} value (0.60) determined by the ratio of the particle bulk density to its real density. The simulated velocity distributions using different ε_{cp} values demonstrated remarkable disparities (Fig. 8(a)), proving the significant influence of ε_{cp} on the particle flow behavior prediction. If the ε_{cp} value is too high/low in the simulation (*e.g.*, $\varepsilon_{cp} = 0.68/0.52$), the CPFD simulation will overestimate/underestimate the particle flow velocity (Fig. 8(a)). Fig. 8(b) shows that ε_{cp} is also crucial in the prediction of the apparent mass flux of the whole system. The simulated k value decreases, while the simulated $\dot{m}$ increases, as ε_{cp} increases. Since ε_{cp} is significant to the gas–solid flow behavior, this parameter in the simulation should be identical to the one determined by the experiment.

The particle-to-wall interaction is expected to be important in such a flow-around process and thus it's the influence of particle-to-wall model parameters on the simulation results is also discussed. In the CPFD model, the normal and tangential momentum restitution coefficient, r_n and r_t, defined as the ratio of the normal and tangential velocities before and after the particle-to-wall collision respectively, are two parameters to depict the particle-to-wall interaction. The variation ranges of these two coefficients are both 0 – 1 in the present simulation and the results are shown in Fig. 9. It seems that r_n and r_t do not show considerable influences on the particle flow field, as the discrepancies among the calculated curves in Fig. 9(a) are within ± 1.2 %. This may be because the particle volume fraction was sufficiently high so that the particles sliding along the wall was overwhelmingly dominate the process rather than the particle collision. r_t shows a comparatively greater influence than r_n but still much less than other parameters (*e.g.*, p_s, β, and ε_{cp}) discussed in the present study.

4.3. Potential deviation of the velocity distribution in the CPFD modeling despite the validated overall calibration parameter

The next noteworthy question is how much deviation of the velocity distribution in the CPFD simulation may be caused when only the con-

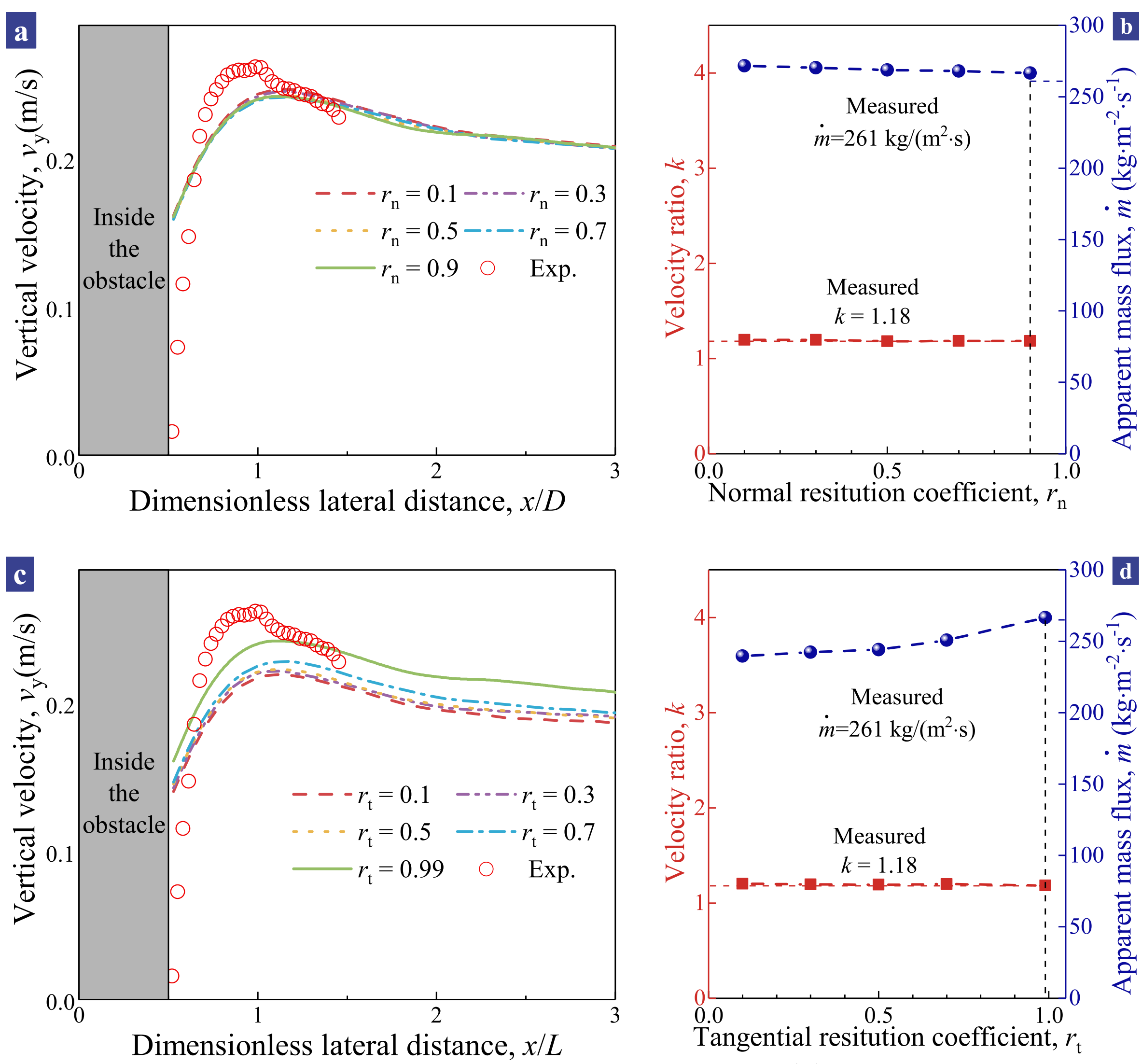

Fig. 9. Influence of the momentum restitution coefficients on the simulation of the dense particle flow behavior. (a), (c) Influence of the normal and tangential restitution coefficient r_n and r_t on the particle velocity distribution simulation. (b), (d) Simulated and measured velocity ratio k and apparent mass flux $\dot{m}$ at different r_n's and r_t's.

ventional overall parameter (*e.g.*, apparent mass flux, $\dot{m}$) is used for model calibration. To answer this question, the sensitivity of the model parameters to the particle velocity distribution and the overall parameter $\dot{m}$ was defined and analyzed. The sensitivity coefficient to the velocity distribution (S_v) was defined as Eq. (11).

$$S_v = \frac{\sqrt{\frac{1}{n}\sum_1^n \sigma_{vi}^2}}{\sigma_q} \tag{11}$$

where σ_q is the relative deviation of a specific parameter q; σ_{vi} the relative deviation of the particle velocity caused by the change of parameter q in mesh i, and n the number of meshes along the lateral direction. Similarly, the sensitivity coefficient to apparent mass flux was defined as Eq. (12).

$$S_m = \frac{\sigma_{\dot{m}}}{\sigma_q} \tag{12}$$

where $\sigma_{\dot{m}}$ is the relative deviation of the apparent mass flux $\dot{m}$ caused by the change of parameter q.

Fig. 10 presents the results of the sensitivity analysis where a 5 % change of the parameter interval was used. The close pack volume fraction is the most important factor in the CPFD simulation of the dense particle flow, while other parameters have similar sensitivity. It is noticed that although p_s has a smaller sensitivity coefficient, it has a larger changing scale reported in existing studies while other parameters have a limited range (*e.g.*, β is limited within 2 – 5). Thus, ε_{cp} and p_s are adopted for further parameter study.

Table 4 lists different combinations of ε_{cp} and p_s values to study the deviation of the velocity distribution simulation. The relative velocity deviation is quantitatively characterized, which is represented by the velocity deviation coefficient Δ as calculated by Eq. (13).

$$\Delta = \sqrt{\frac{1}{n}\sum_1^n \sigma_{vi}^2} \tag{13}$$

The parameter combinations lead to approximately the same simulated $\dot{m}$ (within 271 ± 6 kg/(m^2·s)), while the Δ value is greater than 27 % and even greater than 45 % in some cases, as shown in Table 4. Further comparison is presented in Fig. 11. Although the shapes of the velocity distribution curves computed using the different parameter combinations are similar in the trend, the quantitative results indicate that the CPFD model coefficients only optimized using the overall parameter may lead to considerable error and uncertainties in the particle velocity predictions. This implies that validation of the CPFD model using the overall parameters is not sufficient to prove the accuracy of the particle velocity prediction. It is highly recommended that the simulated velocity distribution is directly verified using the experimental data if the flow field study is desired.

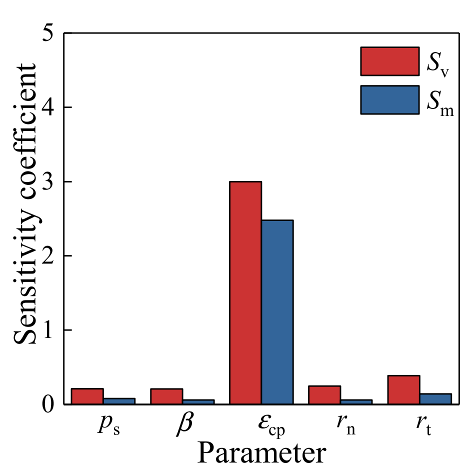

Fig. 10. Sensitivity analysis of the particle stress model, the particle close pack volume fraction, and the momentum restitution coefficients.

Table 4
Predicted apparent mass flux and velocity deviation under different parameter combinations.

Case	Parameter	Apparent mass flux, $\dot{m}$	Velocity deviation, Δ
Standard	$\varepsilon_{cp} = 0.60$, $p_s = 100$	266 kg/(m^2·s)	\
1	$\varepsilon_{cp} = 0.60$, $p_s = 8$	269 kg/(m^2·s)	27.9 %
2	$\varepsilon_{cp} = 0.62$, $p_s = 5$	265 kg/(m^2·s)	39.8 %
3	$\varepsilon_{cp} = 0.64$, $p_s = 3$	269 kg/(m^2·s)	45.6 %

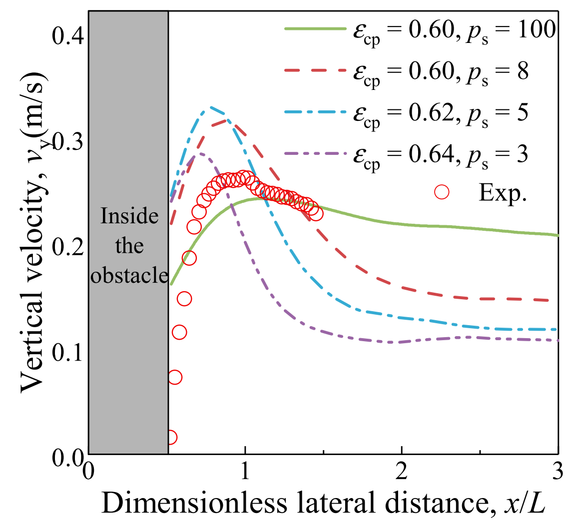

Fig. 11. Velocity distribution simulated using different parameter combinations.

5. Conclusions

In this paper, the simulation of the velocity field of dense particle flows around an obstacle using the computational particle fluid dynamic (CPFD) method was validated and evaluated using the experimental data obtained by the newly-proposed stained-particle image velocimetry technique. The concluding remarks include:

- Three featured flow zones, i.e., the flow stagnant zone, the slip-shear flow zone, and the flow separation zone, were identified in the dense particle flow around an obstacle.
- The CPFD method was capable of accurately predicting the particle flow velocity distribution as well as the overall parameters such as the apparent mass flux if the CPFD model parameters were properly adopted.
- The simulated particle velocity distribution was quite sensitive to the particle pack volume fraction, while particle stress model parameters and particle-to-wall restitution coefficients show less and close sensitivity in the dense particle flow situations.
- Multiple choices of the model parameter combinations could all give accurate apparent mass flux predictions but might lead to very different flow velocity distributions with a prediction error even higher than 45 %. One should directly verify the CPFD simulated flow velocity using the experimental data if the flow field study was desired.

Declaration of Competing Interest

The authors declare the following financial interests/personal relationships which may be considered as potential competing interests:

Yang Zhang reports financial support was provided by National Natural Science Foundation of China. Yang Zhang reports financial support was provided by National Key R&D Program of China. Yang Zhang reports was provided by The Innovation Seed Fund of Shanxi Research Institute for Clean Energy.

Data availability

Data will be made available on request.

Acknowledgment

This study was supported by the National Natural Science Foundation of China (Project NO. 52176116) and the National Key R&D Program of China (Project NO. 2021YFF0600604). The author Y.Z. received financial support from the Innovation Seed Fund of Shanxi Research Institute for Clean Energy, Tsinghua University.

Appendix A. Supplementary data

Supplementary data to this article can be found online at https://doi.org/10.1016/j.cej.2022.139719.

References

[1] E.S. Napolitano, A.D. Renzo, F. Maio, Coarse-grain DEM-CFD modelling of dense particle flow in gas–solid cyclone, Sep. Purif. Technol. 287 (2022), 120591.
[2] S. Wang, Y.S. Shen, Coarse-grained CFD-DEM modelling of dense gas-solid reacting flow, Int. J. Heat Mass Transfer 184 (2022), 122302.
[3] H.D. Zhang, W.B. Li, Q. Ma, Y.W. Zhang, F.L. Lei, Numerical study on influence of exit geometry in gas–solid flow hydrodynamics of HDCFB riser by CPFD, Adv. Powder Technol. 31 (9) (2020) 4005–4017.
[4] D. Wang, T. Jin, K. Luo, J.H. Tan, J.R. Fan, Analysis of the particles-induced turbulence in confined gas-solid fluidized beds by PR-DNS, Int. J. Multiphase Flow 141 (2021), 103655.
[5] P. Traoré, J.C. Laurentie, L. Dascalescu, An efficient 4 way coupling CFD–DEM model for dense gas–solid particulate flows simulations, Comput. Fluids 113 (2015) 65–76.
[6] G.Z. Qiu, J.M. Ye, H.G. Wang, Investigation of gas–solids flow characteristics in a circulating fluidized bed with annular combustion chamber by pressure measurements and CPFD simulation, Chem. Eng. Sci. 134 (2015) 433–447.
[7] X.X. Jiang, S.Y. Wang, Q.H. Zhang, B.L. Shao, H.L. Lu, Granular restitution coefficient-based kinetic theory computations of bubbling fluidized beds, Powder Technol. 394 (2021) 825–837.
[8] W. Bian, X.Z. Chen, J.W. Wang, A critical comparison of two-fluid model, discrete particle method and direct numerical simulation for modeling dense gas-solid flow of rough spheres, Chem. Eng. Sci. 210 (2019), 115233.
[9] J.W. Wang, Continuum theory for dense gas-solid flow: A state-of-the-art review, Chemical Chem. Eng. Sci. 215 (2020), 115428.
[10] Q.Y. Tu, H.G. Wang, CPFD study of a full-loop three-dimensional pilot-scale circulating fluidized bed based on EMMS drag model, Powder Technol. 323 (2018) 534–547.
[11] Y.Y. Wu, X.G. Shi, Y.C. Liu, C.X. Wang, J.S. Gao, X.Y. Lan, 3D CPFD simulation of gas-solids flow in the high-density downer with FCC particles, Powder Technol. 373 (2020) 384–396.
[12] A. Abbasi, P.E. Ege, H. Lasa, CPFD simulation of a fast fluidized bed steam coal gasifier feeding section, Chem. Eng. J. 174 (1) (2011) 341–350.
[13] H.F. Lu, X.L. Guo, Y. Jin, X. Gong, W. Zhao, D. Barletta, M. Poletto, Powder discharge from a hopper-standpipe system modelled with CPFD, Adv. Powder Technol. 28 (2) (2017) 481–490.
[14] Y. Jin, H.F. Lu, X.L. Guo, X. Gong, Application of CPFD method in the simulation of vertical dense phase pneumatic conveying of pulverized coal, Powder Technol. 357 (2019) 343–351.
[15] J.I. Córcoles, A. Acosta-Iborra, J.A. Almendros-Ibáñez, C. Sobrino, Numerical simulation of a 3-D gas-solid fluidized bed: Comparison of TFM and CPFD numerical approaches and experimental validation, Adv. Powder Technol. 32 (10) (2021) 3689–3705.
[16] C.X. Jia, J.W. Li, J.J. Chen, S.S. Cui, H.P. Liu, Q. Wang, Simulation and prediction of co-combustion of oil shale retorting solid waste and cornstalk in circulating fluidized bed using CPFD method, Appl. Therm. Eng. 165 (2020), 113574.
[17] Q.G. Wang, T. Niemi, J. Peltola, S. Kallio, H.R. Yang, J.F. Lu, L.B. Wei, Particle size distribution in CPFD modeling of gas–solid flows in a CFB riser, Particuology 21 (2015) 107–117.
[18] S.H. Zhu, M. Zhang, J.L. Zhang, J.F. Lyu, H.R. Yang, Numerical study on maldistribution of gas–solid flow in multiple-branching limestone-conveying pipelines of circulating fluidized bed, Particuology 46 (2019) 14–21.
[19] D. Chehata, R. Zenit, C.R. Wassgren, Dense granular flow around an immersed cylinder, Phys. Fluids 15 (2003) 1622.
[20] M.S. Buijtenen, M. Börner, N.G. Deen, S. Heinrich, S. Antonyukc, J.A.M. Kuipers, An experimental study of the effect of collision properties on spout fluidized bed dynamics, Powder Technol. 206 (2011) 139–148.
[21] A. Seguin, C. Coulais, F. Martinez, Y. Bertho, P. Gondret, Local rheological measurements in the granular flow around an intruder, Phys. Rev. E 93 (2016), 012904.
[22] J. Baker, F. Guillard, B. Marks, I. Einav, X-ray rheography uncovers planar granular flows despite non-planar walls, Nat. Commun. 9 (2019) 5119.
[23] D. Geldart, Types of Gas Fluidization, Powder Technol. 7 (1973) 285–292.
[24] J.F. Jong, M.S. Annaland, J.A.M. Kuipers, Experimental study on the hydrodynamic effects of gas permeation through horizontal membrane tubes in fluidized beds, Powder Technol. 241 (2013) 74–84.
[25] S. Cloete, A. Zaabout, S.T. Johansen, M.S. Annaland, F. Gallucci, S. Amini, The generality of the standard 2D TFM approach in predicting bubbling fluidized bed hydrodynamics, Powder Technol. 235 (2013) 735–746.
[26] Y.M. Zhang, Y.S. Liang, M. Wang, X.T. Bi, C.X. Lu, Experimental study and CPFD simulation on circumferential flow heterogeneity in a disc-donut catalyst stripper, Chem. Eng. J. 391 (2020), 123567.
[27] J.C. Bandara, C. Jayarathn, R. Thapa, H.K. Nielsen, B.M.E. Moldestad, M. S. Eikeland, Loop seals in circulating fluidized beds – Review and parametric studies using CPFD simulation, Chem. Eng. Sci. 227 (2020), 115917.
[28] A. Seguin, Y. Bertho, F. Martinez, J. Crassous, P. Gondret, Experimental velocity fields and forces for a cylinder penetrating into a granular medium, Phys. Rev. E 87 (2013), 012201.
[29] Y. Amarouchene, J.F. Boudet, H. Kellay, Dynamic Sand Dunes, Phys. Rev. Lett. 86 (2001) 4286.
[30] W. Thielicke, R. Sonntag, Particle Image Velocimetry for MATLAB: Accuracy and enhanced algorithms in PIVlab, J. Open Res. Software 9 (1) (2021) 12.
[31] P. Bartsch, S. Zunft, Numerical investigation of dense granular flow around horizontal tubes: Qualification of CFD model with validated DEM model, Sol. Energy 182 (2019) 298–303.
[32] M.M. Zdravkovich, Flow around circular cylinders – Volume 1: Fundamentals. London: Oxford University Press, 1997.
[33] L.D. Ye, X.J. Liu, D.H. Xia, Flow characteristics of three typical granular materials in near 2D moving beds, Powder Technol. 373 (2020) 220–231.
[34] J.F. Boudet, H. Kellay, Drag Coefficient for a Circular Obstacle in a Quasi-Two-Dimensional Dilute Supersonic Granular Flow, Phys. Rev. Lett. 105 (2010), 104501.
[35] A. Seguin, Y. Bertho, P. Gondret, J. Crassous, Dense Granular Flow around a Penetrating Object: Experiment and Hydrodynamic Model, Phys. Rev. Lett. 107 (2011), 048001.
[36] H.T. Ma, L. He, Large eddy simulation of natural convection heat transfer and fluid flow around a horizontal cylinder, Int. J. Therm. Sci. 162 (2021), 106789.
[37] C. Cheng, J. Werther, S. Heinrich, H.Y. Qi, E.U. Hartge, CPFD simulation of circulating fluidized bed risers, Powder Technol. 235 (2013) 238–247.
[38] F.L. Nie, F.W. Bai, Z.F. Wang, R.G. Yang, A CPFD simulation on the particle flow characteristics in a packed moving bed solar receiver with an added insert, Sol. Energy 224 (2021) 1144–1159.
[39] Q.G. Wang, H.R. Yang, P.N. Wang, J.F. Lyu, Q. liu, H. Zhang, L.B. Wei, M. Zhang, Application of CPFD method in the simulation of a circulating fluidized bed with a loop seal, part I—Determination of modeling parameters, Powder Technol. 253 (2014) 814-821.